Astronomy & Astrophysics manuscript no. lupusco_astroph
October 23, 2017

Squeezed between shells? On the origin of the Lupus I molecular cloud

II. APEX⋆ CO and GASS H I observations

B. Gaczkowski[1], V. Roccatagliata[2,1], S. Flaischlen[1], D. Kröll[1,3], M.G.H. Krause[5,1,3,4], A. Burkert[1,3], R. Diehl[3,4], K. Fierlinger[1,4], J. Ngoumou[1], and T. Preibisch[1]

[1] Universitäts-Sternwarte München, Ludwig-Maximilians-Universität, Scheinerstr. 1, 81679 München, Germany; e-mail: bengac@usm.uni-muenchen.de; e-mail: roccatagliata@arcetri.astro.it
[2] INAF-Osservatorio Astrofisico di Arcetri, L.go E. Fermi 5, 50125 Firenze, Italy
[3] Max-Planck-Institut für extraterrestrische Physik, Postfach 1312, 85741 Garching, Germany
[4] Excellence Cluster Universe, Boltzmannstrasse 2, 85748 Garching, Germany
[5] School of Mathematics & Physics, Private Bag 37, University of Tasmania, Hobart 7001, Australia

Received 14.03.2016; Accepted 13.10.2017

ABSTRACT

Context. The Lupus I cloud is found between the Upper-Scorpius (USco) and the Upper-Centaurus-Lupus (UCL) sub-groups of the Scorpius-Centaurus OB-association, where the expanding USco H I shell appears to interact with a bubble currently driven by the winds of the remaining B-stars of UCL.
Aims. We investigate if the Lupus I molecular could have formed in a colliding flow, and in particular, how the kinematics of the cloud might have been influenced by the larger scale gas dynamics.
Methods. We performed APEX ^{13}CO(2–1) and C^{18}O(2–1) line observations of three distinct parts of Lupus I that provide kinematic information on the cloud at high angular and spectral resolution. We compare those results to the atomic hydrogen data from the GASS H I survey and our dust emission results presented in the previous paper. Based on the velocity information, we present a geometric model for the interaction zone between the USco shell and the UCL wind bubble.
Results. We present evidence that the molecular gas of Lupus I is tightly linked to the atomic material of the USco shell. The CO emission in Lupus I is found mainly at velocities between $v_{\rm LSR}$ = 3–6 km s^{-1} which is in the same range as the H I velocities. Thus, the molecular cloud is co-moving with the expanding USco atomic H I shell. The gas in the cloud shows a complex kinematic structure with several line-of-sight components that overlay each other. The non-thermal velocity dispersion is in the transonic regime in all parts of the cloud and could be injected by external compression. Our observations and the derived geometric model agree with a scenario where Lupus I is located in the interaction zone between the USco shell and the UCL wind bubble.
Conclusions. The kinematics observations are consistent with a scenario where the Lupus I cloud formed via shell instabilities. The particular location of Lupus I between USco and UCL suggests that counter-pressure from the UCL wind bubble and pre-existing density enhancements, perhaps left over from the gas stream that formed the stellar subgroups, may have played a role in its formation.

Key words. radio lines: ISM – ISM: clouds – ISM: kinematics and dynamics – ISM: molecules – ISM: structure ISM: bubbles – individual objects: Lupus I

1. Introduction

Molecular cloud formation is attributed to collisions of large-scale flows in the ISM that can be driven by stellar feedback processes such as UV-radiation, winds, and supernovae (see review by Dobbs et al. 2014). At the interface of the colliding flows, compression, cooling, and fragmentation of the diffuse atomic medium produces cold sheets and filaments that later may become molecular and self-gravitating. Realizations of this general concept include expanding (super-) shells, where an expanding hot bubble collides with the ambient medium (e.g. Krause et al. 2013) and direct collisions of stellar winds (e.g. Calderón et al. 2016).

Such a process might take place between the Upper-Scorpius (USco) H I shell and the Upper Centaurus-Lupus (UCL) wind bubble located in the Scorpius-Centaurus OB-association (Blaauw 1964; de Zeeuw et al. 1999; Preibisch et al. 2002; Preibisch & Mamajek 2008, Sco-Cen). This is the closest site of recent massive star formation to us, at a distance of 110-140 pc only. These shells presumably were created by the feedback of the numerous massive stars in Sco-Cen. In-between those two expanding structures there is the Lupus I cloud which represents a good candidate where we can study how such a collision process forms and influences new dense clouds in the ISM. The distance of the Lupus cloud complex is about 140 pc, as discussed in detail by Comerón (2008). Additional details about the region and the Lupus I cloud can be found in Gaczkowski et al. (2015) (Paper I hereafter).
Molecular line observations of Lupus I with different CO isotopes and other high-density tracers have been performed by sev-

⋆ This publication is based on data acquired with the Atacama Pathfinder Experiment (APEX). APEX is a collaboration between the Max-Planck-Institut fur Radioastronomie, the European Southern Observatory, and the Onsala Space Observatory.

eral groups over the past two decades. Most of them have spatial resolutions of several arcminutes, i.e. ∼ 0.1 pc at the distance of Lupus I of ∼ 140 pc. Tachihara et al. (1996) observed the entire Lupus I cloud in the ^{13}CO(1–0). They estimated the cloud mass to be ∼ 1200 $M_\odot$ and discovered the molecular outflow of IRAS source 15398–3359. Hara et al. (1999) have studied 12 cores in Lupus I in the C^{18}O(1–0) line. The spatial resolution of the NANTEN telescope is 2.7′, while their grid spacing was 2′. They derived column densities, temperatures, and sizes for the cores, and estimated their total mass to be 152 $M_\odot$. This represents 46% of their total C^{18}O(1–0) emitting gas mass. Vilas-Boas et al. (2000) found 15(14) condensations in C^{18}O(1–0)(^{13}CO(1–0)) highlighting the recent star formation activity in Lupus I. A large-scale ^{12}CO(1–0) survey of Lupus I has been performed by Tachihara et al. (2001). They find a velocity gradient along the long axis of Lupus I from 4 km s^{-1} in the south to 6 km s^{-1} in the north. Tothill et al. (2009) analyzed Lupus I in both CO(4–3) and ^{13}CO(2–1). They found several possible signs of interaction between Lupus I and the USco H I shell. Benedettini et al. (2012) found eight dense cores in Lupus I using high-density molecular tracers at 3 and 12 mm. They reported the presence of velocity gradients in the cloud and several velocity components along the line-of-sight. Finally, Benedettini et al. (2015) observed the southern part of the main filament in CS(2–1) and they found several sub-filaments in velocity space that correspond to sub-filaments they have identified in their *Herschel* column density maps.

In our dust analysis presented in Paper I we found a double peaked PDF which suggests a scenario of external compression of Lupus I from USco and/or UCL.
In this work, we follow up on this suggestion, and present ^{13}CO(2–1) and C^{18}O(2–1) observations of three distinct regions within the Lupus I cloud with a high angular and spectral resolution of ≈ 30″ and ≈ 0.1 km s^{-1}, respectively. We present the analysis of the observational data and the comparison to the available H I data. From those we create a geometrical model for the interaction zone of shell and bubble. We show that the collision scenario is a plausible explanation of the observational data and the creation of Lupus I with other factors likely having played a role as well.

2. Observations and data reduction

2.1. APEX CO observations

The CO line observations of Lupus I were performed with the APEX telescope (Güsten et al. 2006) using the APEX-1 receiver of the Swedish Heterodyne Facility Instrument (SHeFI; Vassilev et al. 2008). The observations were carried out on 18th and 20th August 2014 (PI: B. Gaczkowski; Program ID: 093.F-9311(A)). Lupus I was observed simultaneously in the ^{13}CO(2–1) (rest frequency ν_0^{13} = 220.398677 GHz) and C^{18}O(2–1) (ν_0^{18} = 219.560357 GHz) line. Three scans across the cloud were performed, as shown in Figure 1. These were chosen based on our previous dust analysis to obtain representative samples of the conditions along the whole filament. The observing mode was *"on-the-fly"* and the map parameters for each cut are listed in Table 1. The scanning direction was along the long side of a cut. The velocity resolution of the spectra is Δv = 0.1 km s^{-1} and the rms noise ranges between ≈ 0.05–0.1 K for both lines. The perceptible water vapor (PWV) during the observations was between 1.5 and 2 mm. Each cut contains about 620 spectra.

The data reduction was done using the `CLASS` package of the IRAM `GILDAS` software[1]. The antenna temperature T_A was converted into a main-beam temperature $T_{mb} = T_A/\eta$, adopting a main-beam efficiency of η = 0.75 for APEX-1[2]. All spectra were baseline subtracted. Finally, for each line and cut, a map (or `lmv` cube) was produced with the `XY_MAP` task which convolves the data with a Gaussian of one third of the beam. The final angular resolution is 30.1″ and the pixel size is 14.3″.

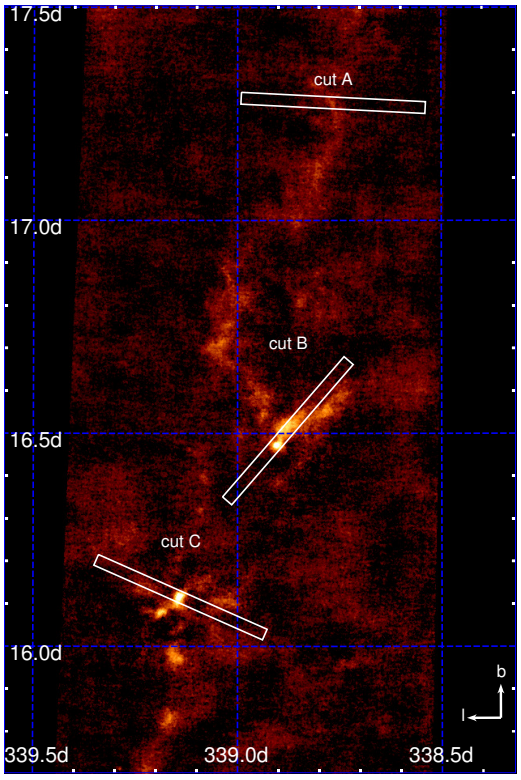

Fig. 1. Setup of the APEX-1 ^{13}CO(2–1) and C^{18}O(2–1) observations of Lupus I. Along each of the three cuts A, B, and C an on-the-fly map was obtained simultaneously in both lines. The size of each map is marked with a white box. The background image is the LABOCA continuum map (see Paper I). The Galactic coordinate system is indicated.

2.2. GASS H I data

The atomic hydrogen data of the entire Sco-Cen region used in our study are part of the second data release of the GASS H I survey (Kalberla et al. 2010). This has a spatial resolution of 16.2′ which corresponds to a length scale of 0.7 pc at the distance of Lupus I. The velocity resolution is 1 km s^{-1} and the rms noise is 55 mK.
In order to characterise the HI shell around Upper Scorpius (the Upper Scorpius loop) and relate it to the Lupus I cloud, which forms part of the filaments of the shell rim, we fitted an expanding homogeneous spherical shell to the HI data. In addition we used Na I absorption data in the foreground of stars with know distances from Hipparcos measurements, using the same shell model as for the HI data. This follows an analysis approach presented elsewhere (Pöppel et al. 2010; Welsh et al. 2010). The parameters of our expanding-shell model are:

– distance to the center of the shell D_0

[1] `http://www.iram.fr/IRAMFR/GILDAS`
[2] `http://www.apex-telescope.org/telescope/efficiency`

Table 1. Details of the molecular line maps obtained for Lupus I with APEX-1. The first column gives the name of the cut, the second and third column give the x and y size of the whole map. Column four gives the length of the cut, columns five and six the position of the center of the map, and the last column gives the number of pixels that contain a spectrum. These parameters are valid for both the ^{13}CO and C^{18}O maps of one cut. The angular resolution of the maps is 30.1″ and the pixel size 14.3″. The three cuts share a common OFF-position at RA = 15:44:23.605 and Dec = −33:39:00.68.

Cut	Map size X	Map size Y	Length	Center RA$_{J2000}$	Center Dec$_{J2000}$	No. of spectra
A	21′	18′	26′	15:40:05.35	−33:36:44.4	617
B	26′	6′	24′	15:42:49.80	−34:08:37.8	618
C	13′	24′	26′	15:44:57.60	−34:17:13.3	620

- galactic longitude l_0 of the shell center
- galactic latitude b_0 of the shell center
- radius of the inner edge of the shell r_{in}
- thickness of the shell Δr
- density of hydrogen atoms n_H in the shell assumed to be spatially constant
- expansion velocity of the shell $V_{\rm exp}$
- bulk velocity of interstellar medium in the Sco-Cen region V_0.

The distance to the shell centre D_0 was determined from a multi-parameter fit to the absorption data, yielding
$D_0 = 138 \pm 26$ pc. Here, the uncertainties have been propagated from the uncertainties in the distance measurements of the stars. For the fit to the HI data, we transformed this model from 3D Cartesian space (x, y, z) into (l, b, v) space, added the HI Milky Way model of Kalberla et al. (2007) as a large-scale background, and optimised model parameters fitting to the HI data by a χ^2 minimization. The set of best fitting parameters are:
$l_0 = 347 \pm 0.5$ deg, $b_0 = 25 \pm 0.5$ deg, $r_{\rm in} = (12.3 \pm 0.7)$ deg,
$\Delta r = 2.7 \pm 0.3$ deg, $n_{\rm H} = 6 \pm 2 {\rm cm}^{-3}$, $V_{\rm exp} = (7 \pm 1)$km/s,
$V_0 = 8 \pm 1$km/s.
Uncertainties are quoted as 1 σ. The total mass of hydrogen in the shell is 11 000 ± 6000 $M_\odot$. This is similar to the value determined by Pöppel et al. (2010) from lower quality data.
The mass determination has additional significant systematic uncertainties, as the shell is not detected on the far side. On the near side, a spherical shape is plausibly seen, but the galactic foreground adds uncertainties.

3. Results

The individual spectra are complex, with a variety of different line profiles. The velocity of the emitting gas ranges from $v_{\rm LSR}$ = 3.2 to 6.8 km s^{-1}. The maps have been convolved with a Gaussian of two pixels or approximately one beam. All observed spectra can be found in Appendix A in Figures A.2-A.7. The main ^{13}CO emission in **cut A** is at velocities of $v_{\rm LSR}$ = 5.5–6.2 km s^{-1} with the highest intensities between 5.9 and 6.1 km s^{-1}. The emission is concentrated to the center of the cut and extends to about 10′ around the center in the channels with highest intensities. Detectable C^{18}O emission region is limited to about 2′ around the very center of the cut.
The highest intensities of the three cuts are found in **cut B**. The bulk of the C^{18}O emission lies at the same velocity range as the ^{13}CO emission. It is concentrated on the center of the cut and no emission is found at either edge.
Within **cut C** several spatially distinct emission regions can be seen in ^{13}CO and C^{18}O. In contrast to the other two cuts, the ^{13}CO and C^{18}O emission peaks do not overlap, but are located at opposite ends of the cut. C^{18}O emission is found at three positions within the cut.

The average ^{13}CO and C^{18}O spectrum has been then computed for each cut and they are shown in Figure 2. The solid lines represent the average ^{13}CO spectrum and the dotted lines the average C^{18}O spectrum multiplied by three. Cut A shows the lowest intensities of all three cuts in both lines. The averaged ^{13}CO line is very broad and asymmetric towards velocities lower than the velocity of the peak, i.e. $v_{\rm LSR}$ = 5.75 km s^{-1}. The peak intensity of the ^{13}CO line is 1.22 K. The ^{13}CO line of cut B is the most narrow and has the highest peak intensity of all three cuts with a value of 4.44 K at $v_{\rm LSR}$ = 5.02 km s^{-1}. For cut C the ^{13}CO line also peaks at $v_{\rm LSR}$ = 5.02 km s^{-1} with a peak intensity of 3.26 K. The averaged C^{18}O lines of cut B and cut C both peak at $v_{\rm LSR}$ = 5.13 km s^{-1} and have a peak intensity of 1.34 and 0.74 K, respectively.

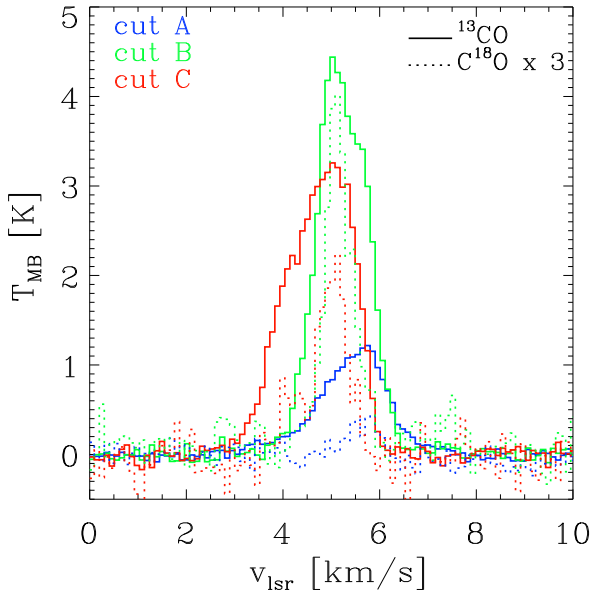

Fig. 2. Average ^{13}CO and C^{18}O spectra of the three cuts. The integrated intensities (for $v_{\rm LSR}$ = 0–10 km s^{-1}) of the ^{13}CO lines are 1.96, 5.69, and 5.55 K km s^{-1} for cut A, B, and C, respectively. Those of the C^{18}O lines are 1.22, and 0.50 K km s^{-1} for cut B and cut C, respectively.

4. Analysis

We first calculate the optical depth, excitation temperature, and column density under the assumption of local thermodynamical equilibrium (LTE). A multi-gaussian fit determines the different velocity components of the observed spectra. We finally search for a non-thermal contribution to the spectra.

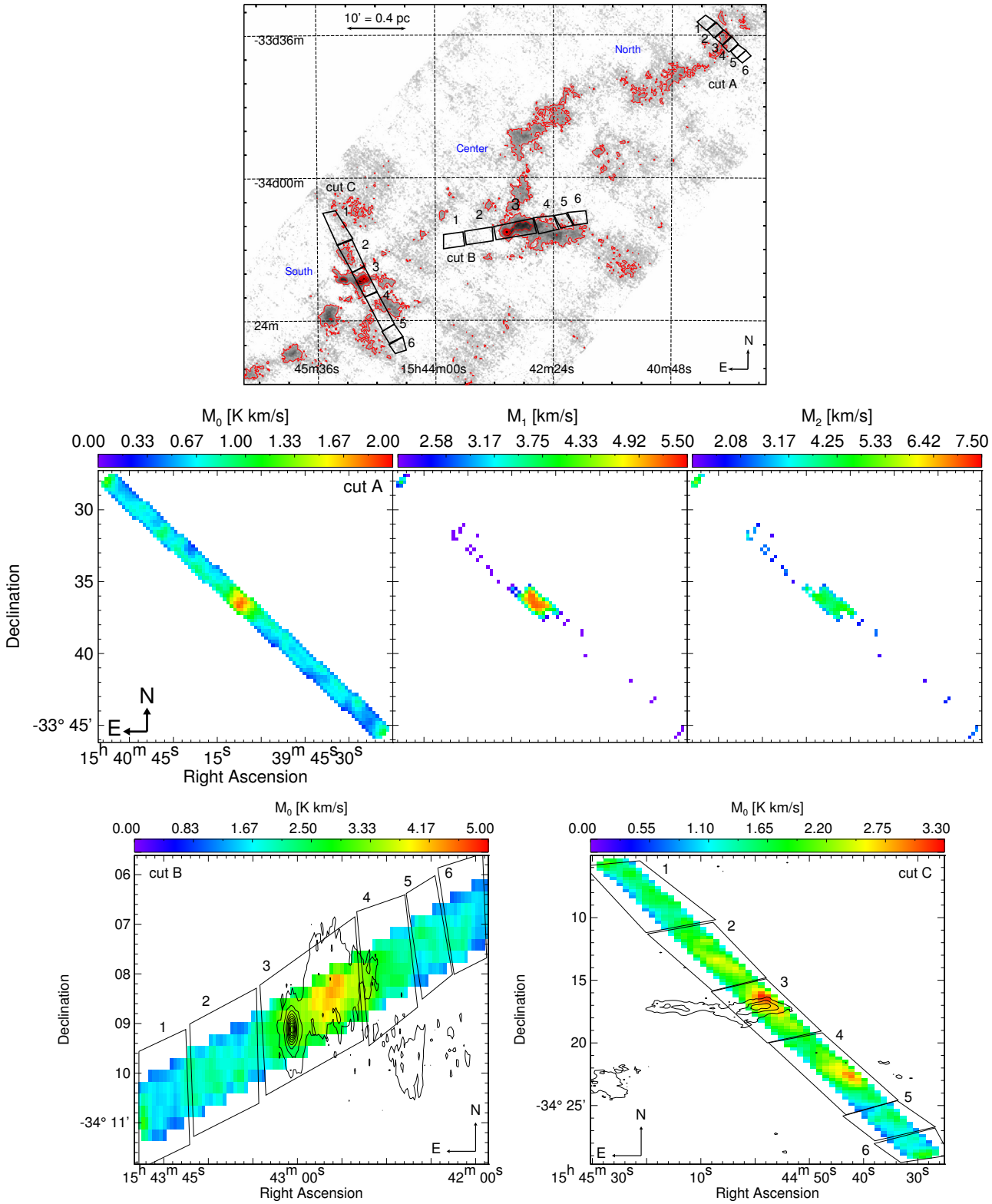

Fig. 3. *Top Left:* Dust column density map from LABOCA with red contour levels of 0.3, 1, 1.7, 2.3, and 3×10^{22} cm^{-2}. Integrated C^{18}O(2–1) intensity maps of cut A, B, and C (*Top Right* and *Bottom* figures, respectively). The six boxes into which each cut was divided are shown, as well as the contours of the LABOCA 870 μm continuum emission. Levels are from 10%–100% of the peak intensity of 1.37 Jy/beam.

4.1. LTE density analysis

Spectra with a S/N > 4 were selected to compute optical depth, excitation temperature, and column density. This assures that both lines are clearly detected. For our analysis we assume LTE conditions: The excitation temperature T_{ex} is equal to the kinetic temperature of the gas and the same for all transitions and both CO isotopologues. This assumption should hold when the temperature distribution along the line-of-sight is uniform.

The equations and constants used for the calculations of the excitation temperature and the column density in this section can

be found in Appendix A.
The H_2 column density map calculated from dust emission (see Paper I) showed that almost all of Lupus I lies below 1×10^{23} cm^{-2}. Therefore, C^{18}O is optically thin (Carlhoff et al. 2013). The optical depth of the ^{13}CO gas is computed (see e.g. Myers et al. 1983; Ladd et al. 1998) using the relation:

$$\tau_{13} = \Gamma \times \tau_{18} \quad (1)$$

with $\tau_{13} = \tau(^{13}\mathrm{CO})$, $\tau_{18} = \tau(\mathrm{C}^{18}\mathrm{O})$ and $\Gamma = [^{13}\mathrm{CO}]/[\mathrm{C}^{18}\mathrm{O}]$ is the relative abundance ratio of the given isotopologues. Here we adopt a constant abundance ratio of $\Gamma = 7.3$ (Wilson & Rood 1994, local ISM). Then the optical depth τ_{13} can be approximated by the intensity ratio of the lines

$$\frac{T^{13}_{\mathrm{mb}}(v)}{T^{18}_{\mathrm{mb}}(v)} = \frac{1 - \exp(-\tau_{13})}{1 - \exp(-\tau_{13}/\Gamma)} \quad (2)$$

with $T^{13}_{\mathrm{mb}}(v)$ and $T^{18}_{\mathrm{mb}}(v)$ the main-beam temperature of the corresponding line at velocity channel v. In principle this relation is valid for every velocity channel. Here, we chose $T^{18}_{\mathrm{mb}}(v) = T^{18}_{\mathrm{peak}}$ the peak brightness temperature of the C^{18}O line. Then $T^{13}_{\mathrm{mb}}(v) = T^{13}_{\mathrm{peak}}$ is the corresponding brightness temperature of ^{13}CO at the velocity channel of the C^{18}O peak intensity. The resulting optical depth maps for C^{18}O are shown in the left panels of Figure A.1. The optical depth τ_{18} is in the range 0.3 to 1 for most of the cloud, with isolated peaks up to about 1.5.
The **excitation temperatures** are computed using the optically thin C^{18}O line (equations A.1 and A.2 in the appendix). The resulting T_{ex} maps are displayed in the middle panels of Figure A.1. The mean excitation temperatures for cuts A, B, and C are 16.8, 14.7, and 14.7 K. Our excitation temperatures calculated in our analysis are comparable to previous findings from different CO and molecular observations of Lupus I. With Equation A.3 we compute the C^{18}O **column density**, and find H_2 column density assuming a constant abundance ratio of $[\mathrm{C}^{18}\mathrm{O}]/[\mathrm{H}_2] = 1.7 \times 10^{-7}$ (Haworth et al. 2013) for the three column density maps shown in the right panels of Figure A.1.
The column density distribution (called $N_{H[CO]}$) has been compared to the total column density obtained from the dust ($N_{H[FIR\,dust\,em.]}$ from Paper I).
We fit a gaussian to the distribution of the ratio between the $N_{H[CO]}$ and $N_{H[FIR\,dust\,em.]}$ first considering all the cuts together, then among each of the 3 cuts. The distribution peaks at 0.8 with a standard deviation of 0.3. In general, the column density from CO gas emission is found lower than the column density from dust emission. Along cut A the ratio between gas and the dust column density peaks at 1 with a standard deviation (σ) of 0.7, σ=0.3 for cut B, while for cut C the peak of the ratio is not clearly identified as the other 2 cuts.

4.2. Determination of different velocity components and non-thermal motions

In this section we present a detailed analysis of the different CO velocity components.
Each cut was divided into six boxes as shown in Figure 3. The derived position-velocity (PV) diagrams are shown in Figure 4. Figure 5 shows the average ^{13}CO (top row) and C^{18}O spectrum (bottom row).
Using a multi-component (up to three) Gaussian fit of the spectra (Figures A.2 to A.7), we computed the peak position and FWHM for each component fo the ^{13}CO (top row) and C^{18}O (see Table 2 for more details). We conclude from this that a velocity decrease

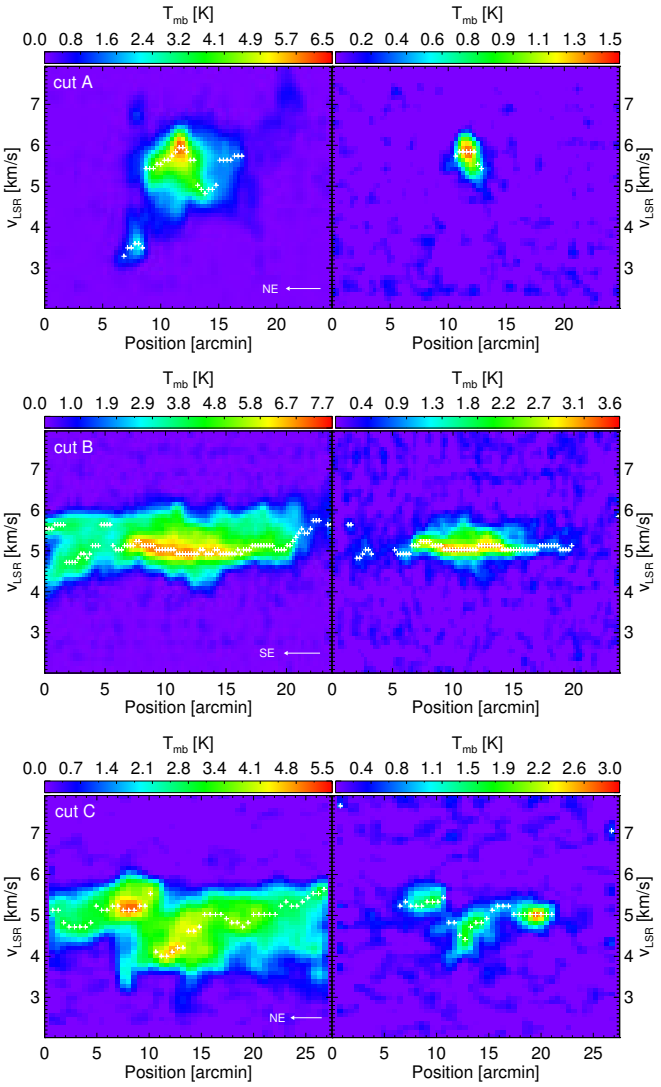

Fig. 4. Position-velocity diagrams of cut A, B, and C (from top to bottom) in ^{13}CO(2–1) (left panel) and C^{18}O(2–1) (right panel) along a line through the middle of the cut. The x-axis gives the position along this line. The white arrow in the bottom right corner of the left panels indicates the orientation of the cut in the Celestial coordinate frame. The white crosses mark the velocity of the peak intensity at each x-position. The cutoff is set to 1 K in ^{13}CO(2–1) for all three cuts and 0.5 K in C^{18}O(2–1) for cuts B and C. The C^{18}O(2–1) cutoff for cut A is 0.3 K. All maps have been convolved with a Gaussian of two pixels or approximately one beam.

from cut A to cut C is seen. No clear trend is seen in linewidths, suggesting a homogeneous level of turbulence.
The **non-thermal velocity dispersion** of the gas has been then derived from the measured linewidth, subtracting the thermal component. Following the standard assumption that the thermal and non-thermal components are independent (see e.g. Myers 1983), the non-thermal velocity dispersion σ_{NT} is

$$\sigma_{\mathrm{NT}} = \sqrt{\frac{\Delta v^2}{8 \ln 2} - \frac{k_{\mathrm{B}}\, T_{\mathrm{kin}}}{m}} \quad (3)$$

with Δv the measured linewidth, k_{B} the Boltzmann constant, T_{kin} the kinetic gas temperature (here we adopt 10 K), and m the mass of the observed molecule ($m_{^{13}\mathrm{CO}} = 29$ u, $m_{\mathrm{C}^{18}\mathrm{O}} = 30$ u). Dividing σ_{NT} by the isothermal sound speed $c_{\mathrm{s}} = 0.19\,\mathrm{km\,s^{-1}}$ for a 10 K ISM gas, gives a direct measure of non-thermality of the

Table 2. Values of peak positions ($v_{p_i}^G$) and FWHM (Δv_i^G) of the different components in each averaged spectrum of one box within a cut determined from multi-component Gaussian fitting (see Figures A.2 to A.7).

Box	$C^{18}O$ [km s^{-1}]				^{13}CO [km s^{-1}]					
#	$v_{p_1}^G$	Δv_1^G	$v_{p_2}^G$	Δv_2^G	$v_{p_1}^G$	Δv_1^G	$v_{p_2}^G$	Δv_2^G	$v_{p_3}^G$	Δv_3^G
cut A										
1	–	–	–	–	5.45	1.03	3.68	0.97	6.76	0.53
2	5.65	0.55	–	–	5.60	0.83	4.96	1.73	–	–
3	5.77	0.76	–	–	5.95	0.76	5.27	1.44	–	–
4	5.45	0.94	–	–	5.63	1.22	4.86	0.56	–	–
5	–	–	–	–	5.86	0.88	4.96	1.00	–	–
6	–	–	–	–	5.76	0.87	4.75	0.87	–	–
Ø	5.62	0.75	–	–	5.71	0.93	4.75	1.10	6.76	0.53
cut B										
1	5.03	1.08	–	–	4.71	0.97	5.62	0.48	–	–
2	5.14	0.63	–	–	5.13	1.00	5.75	0.30	–	–
3	5.14	0.66	–	–	5.15	1.19	–	–	–	–
4	5.13	0.63	–	–	5.00	0.53	5.64	0.74	–	–
5	5.25	0.81	–	–	5.34	1.21	–	–	–	–
6	–	–	–	–	–	–	5.62	1.10	–	–
Ø	5.14	0.76	–	–	5.07	0.98	5.66	0.66	–	–
cut C										
1	4.93	0.55	–	–	4.97	1.09	–	–	–	–
2	5.35	0.57	4.51	1.31	5.25	1.12	4.02	0.90	–	–
3	4.86	0.65	4.22	0.55	–	–	4.50	1.51	–	–
4	5.04	0.45	–	–	5.15	0.88	4.34	1.31	–	–
5	–	–	–	–	5.35	0.63	4.50	1.12	3.28	0.44
6	–	–	–	–	5.51	0.60	4.35	1.41	3.51	0.29
Ø	5.05	0.56	4.37	0.93	5.25	0.86	4.34	1.25	3.40	0.37

component. For the measured linewidths of ^{13}CO in the three cuts, this indicator is between 2.0 and 4.5, suggesting that the gas would be supersonic. However, correcting the ^{13}CO linewidth for opacity broadening due to its higher optical depth $\tau_{13} > 1$–2 (Phillips et al. 1979), while $C^{18}O$ $\tau_{18} < 1$, this yields a lower indicator value of σ_{NT}/c_s between 0.9 and 1.8. Hence, most of the $C^{18}O$ gas within the three cuts is in the trans-sonic regime ($1 < \sigma_{NT}/c_s < 2$). Typically, the gas of a quiescent cloud resides in the sub-sonic regime as found e.g. by Hacar & Tafalla (2011) for L1517. In Lupus I this signature of turbulence might have been imprinted on the gas by the large-scale interaction with the H I shell of USco and the wind-blown bubble of UCL.

5. Comparison between CO and HI

In this section we present a comparison between CO and H I data and a geometrical model to check the scenario that Lupus I is located in the interaction zone of the USco H I shell and the UCL wind bubble.

Figure 6 shows for v_{LSR} = 0–8 km s^{-1} an H I column density map of Lupus I, together with $C^{18}O$(1–0) emission (Hara et al. 1999) for the same velocity range as the CO emission. Although the peak velocities of HI and CO agree, the H I and CO emission do not spatially agree with each other: the highest H I column density is located at the north-western end of Lupus I, while in the central and the southern part of Lupus I there is less H I emission, roughly by a factor of 1.5. Between $b = 15°30'$–$17°$ and $l = 338°30'$– $339°30'$ the deficit in H I emission around the center-south of Lupus I has the form of a little hole. The H I emission, in general, is enhanced at the Galactic west side of Lupus I and has a deficit on its east side, with an average $\langle N_H \rangle = 5.5 \times 10^{20}$ cm^{-2}. The atomic to molecular ratio is poorly-defined, given the large uncertainties in the these values. Benedettini et al. (2015), for example, reported a ratio of $\langle N_H \rangle / \langle N_{H_2} \rangle \approx 1.6$ calculated from their *Herschel* column density maps and the H I data of de Geus (1992).

The particular distribution of CO and H I shows that Lupus I marks a transition region between the molecular and atomic phase of H I. At those places in the cloud where the atomic hydrogen emission is decreased, the molecular emission is enhanced and vice versa (see Figure 6). Our analysis shows that the $C^{18}O$ emission is significantly higher in the center and the south of Lupus I. We conclude that the north has not built enough dense molecular material yet to start the star formation process. The lower dust column densities seen there coincide with a higher fraction of atomic material. Correspondingly, $C^{18}O$ emission is strongest in the central and southern parts of Lupus I where the H I emission has a deficit and active star formation and high CO column densities ($N(H_2) \approx 10^{22}$ cm^{-2}) can be seen.

Heiner et al. (2015) have created synthetic H I and CO observations from a numerical simulation of decaying turbulence in the thermally bistable neutral medium. They found a power-law tail in the column density PDF when molecular clouds have formed. This tail, however, only appears in the PDFs of the molecular material and not the H I. Hence, they conclude that the molecule formation is directly correlated with gravitational infall. As the dust PDF of the northern part of Lupus I (see Paper I) does not show a power-law tail, the gravitational infall might not yet be

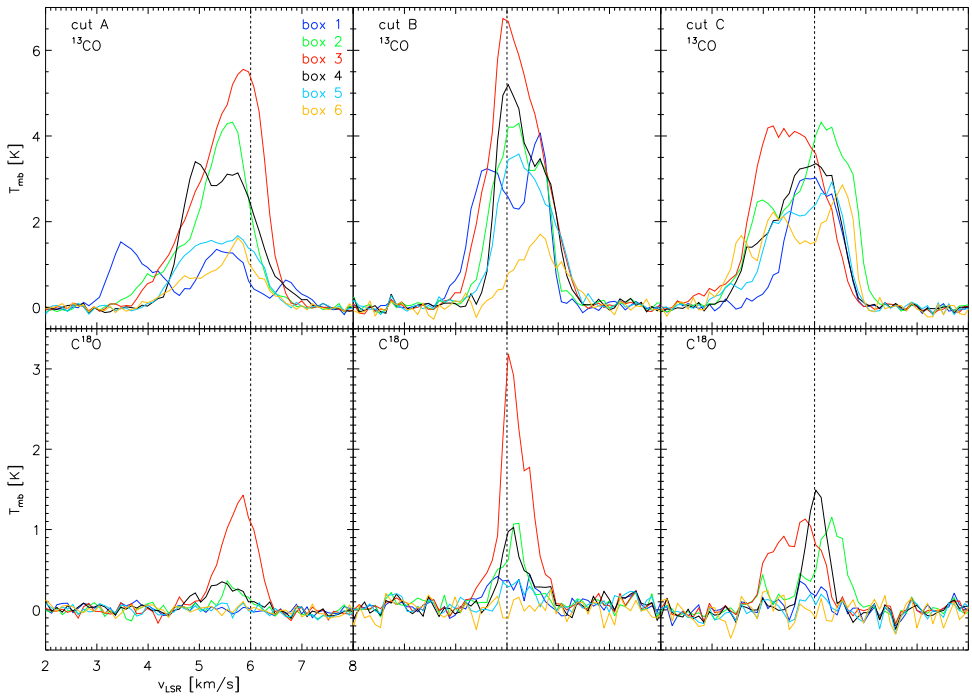

Fig. 5. Averaged spectra within the six boxes into which each cut was divided. The top row shows the average ^{13}CO(2–1) spectra; the bottom those of C^{18}O(2–1). Each column represents one of the three cuts. The different colors denote the six boxes from 1 to 6. The vertical dashed line marks for orientation $v_{\rm LSR} = 6\,{\rm km\,s^{-1}}$ for cut A and $v_{\rm LSR} = 5\,{\rm km\,s^{-1}}$ for cuts B and C.

strong enough to convert as much atomic material into molecular in the center-south.

5.1. Geometrical model for the interaction zone

We construct a geometrical model with the observer located in the origin of the coordinate system which is a 3D Cartesian Galactic coordinate system with

$$\begin{pmatrix} x \\ y \\ z \end{pmatrix} = \begin{pmatrix} r\,\sin\theta\,\cos\phi \\ r\,\sin\theta\,\sin\phi \\ r\,\cos\theta \end{pmatrix} \tag{4}$$

where $\theta = 90° - b$, $\phi = l$, r is the distance, b and l the galactic latitude and longitude, respectively. The x-axis points to the Galactic center. Both, H I shell and wind bubble are represented by a sphere. We place the center of the USco sphere at $(l, b) = (347°, +25°)$ and a distance of 145 pc. A radius of $\sim$ 30 pc is the inner shell radius from our H I model fit (details in Kröll 2018) as observations suggest that Lupus I is located closer to the inner edge of the shell.
We estimate the average projected position of the B-stars southwest of Lupus I that might be responsible for the wind bubble (see Paper I) to be $(l, b) = (331°, +12°)$. This also agrees with the center of a circle in the ROSAT image enclosing the X-ray emission in this region (c.f. Fig. 7 in Paper I). The average distance to the stars of the UCL subgroup is about 5 pc smaller than that to USco (de Zeeuw et al. 1999) and thus we place the center of our UCL sphere model at 140 pc.
Our UCL wind bubble is thus on the near side of the USco H I shell. Figure 7 shows the of the model in three perspectives, at the stage at which the UCL bubble touches the USco sphere. In Figure 7 all points on the surface of the USco sphere that have a model velocity between 3–6 km s^{-1} are marked in cyan. This represents the CO velocity range we have observed in Lupus I. The UCL wind bubble (i.e. the sphere of influence of the massive stars in UCL) interacts with the USco H I shell at positions that have a similar gas velocity to Lupus I.
The Lupus I cloud and the USco H I shell have similar observed velocities and thus it seems reasonable that Lupus I is expanding with the USco shell.
In our purely geometrical model, which does not accurately reflect the physics and the resulting complex morphologies present in the Sco-Cen region, the UCL wind bubble and the USco H I shell nevertheless intersect at velocities consistent with our observations of Lupus I. Therefore, the observational data are in agreement with the idea that Lupus I is in an interaction zone between the USco H I shell and the UCL wind bubble. Moreover, this model comparison indicates that Lupus I is expanding with the USco shell and that the cloud is located at the inner edge of the H I shell.

6. The surroundings of Lupus I and the interaction with USco and UCL

Figure 8 shows the USco H I shell as observed today. A H I column density map of USco and the surroundings of Lupus I is shown in the top panel, together with the dust emission at 850 μm and the CO(1–0) emission from *Planck*, and early B-type stars in USco and UCL. Our model fit to the H I data yields a shell expansion velocity of $\sim$ 7 km s^{-1} and a thickness of $\sim$ 6 pc. The current inner and outer radius is $\sim$ 30 pc and $\sim$ 36 pc, respectively (indicated by the two black circles in Fig. 8). East and west of Lupus I there are clear H I voids and the atomic material is concentrated in the same area as the dust. A further zoom on Lupus I (right panel of Fig. 8) reveals a complicated distribution of atomic, molecular, and dust material. Whereas the CO emission is always found in regions of dust emission, there are several areas within the USco shell ridge where there is H I emission but neither dust nor CO are detected. The layering of atomic and

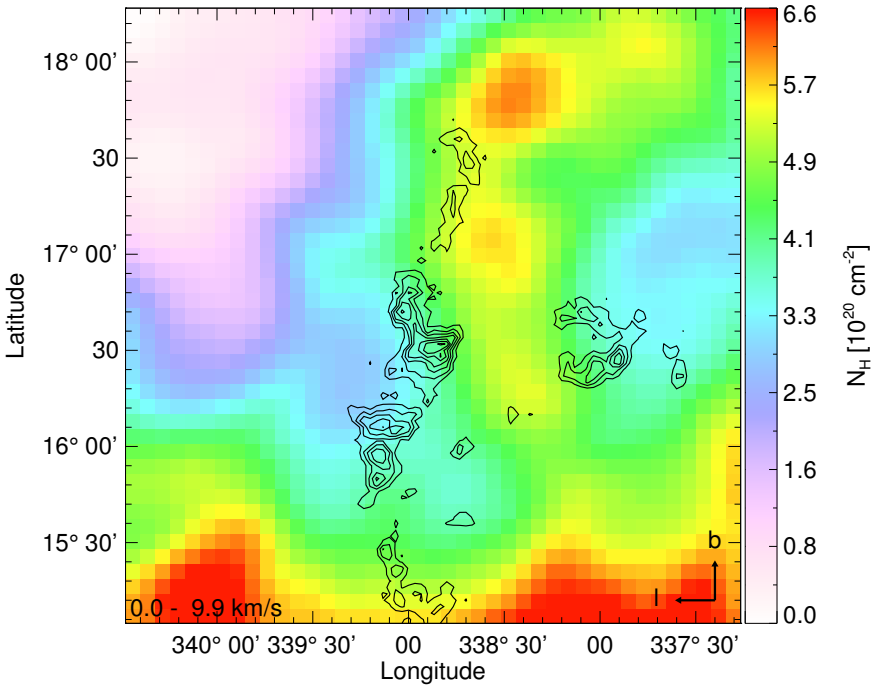

Fig. 6. H I column density map calculated from the integrated emission for $v_{\rm LSR}$ = 0–10 km s^{-1}. Black contours show the integrated C^{18}O(1–0) emission observed by Hara et al. (1999).

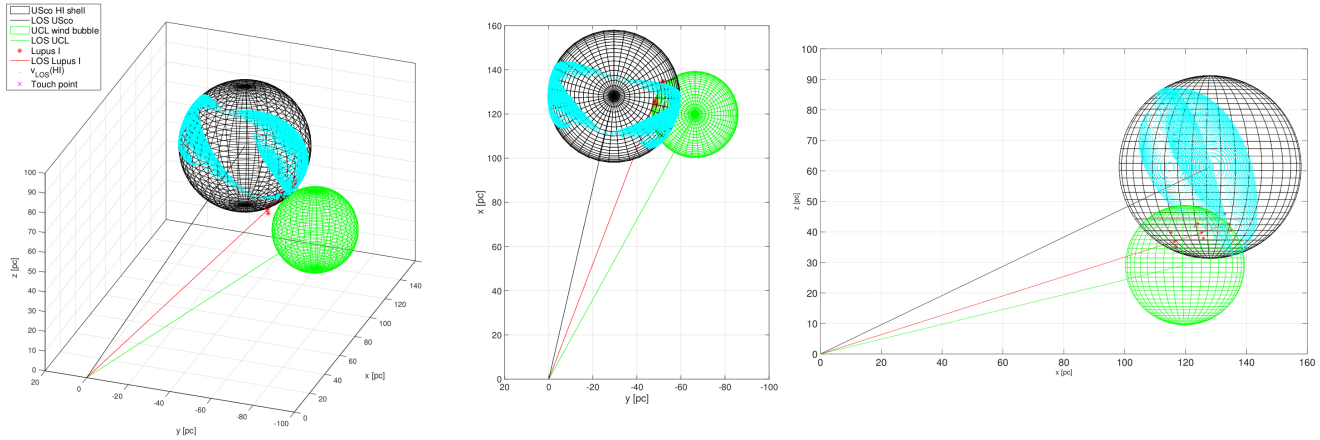

Fig. 7. Geometrical model of the possible interaction zone between the USco H I shell (black sphere) and the UCL wind bubble (green sphere). The observer is located in the origin of the coordinate system. The position of Lupus I is marked by three red asterisks that represent the top, middle, and bottom of the main filament, respectively. The cloud is plotted at three different distances of 150, 140, and 130 pc along the red line which is the line-of-sight from us to Lupus I. The black and the green solid lines are the line-of-sight from the observer to the corresponding sphere. The cyan dots mark those positions on the USco shell that have line-of-sight velocities between 3 and 6 km s^{-1}, i.e. similar to Lupus I (the white gaps are an effect of the grid model used in the calculations). They were calculated from the model fit to the H I data of USco. The magenta cross marks the touch point between the USco and the UCL sphere. The projections are show in the different panels.

molecular material, as can be seen in Lupus I (molecular gas, traced by CO, is surrounded by H I), is also found in some other locations in the shell around Lupus I. In the part of the shell where Lupus I is located, the molecular gas is found preferably behind the atomic gas, i.e. closer to the inner edge of the shell. However, local turbulence and inhomogeneities apparently lead to complex configurations.

The comparison of our CO to H I data showed that both fall into the same velocity range. If thus Lupus I is co-moving with the atomic gas in the shell its formation within the shell wall seems plausible. Dawson et al. (2011) found that expanding supershells are capable of sweeping up big amounts of gas from the ISM. Increased density within their walls leads to very short chemical timescales. They estimate a transition timescale from atomic to molecular material of $\sim 10^6$–10^7 yr (see also Koyama & Inutsuka 2000; Bergin et al. 2004; Heitsch & Hartmann 2008; Clark et al. 2012). The estimated age of the USco shell is $\sim$ 5 Myr and hence it should have had sufficient time to accumulate locally enough atomic gas to convert it into molecular gas at the position of Lupus I. From the dust analysis described in Paper I we found that the total cloud (gas + dust) mass of Lupus I is only $\sim$ 170 M$_\odot$. This is at least two orders of mag-

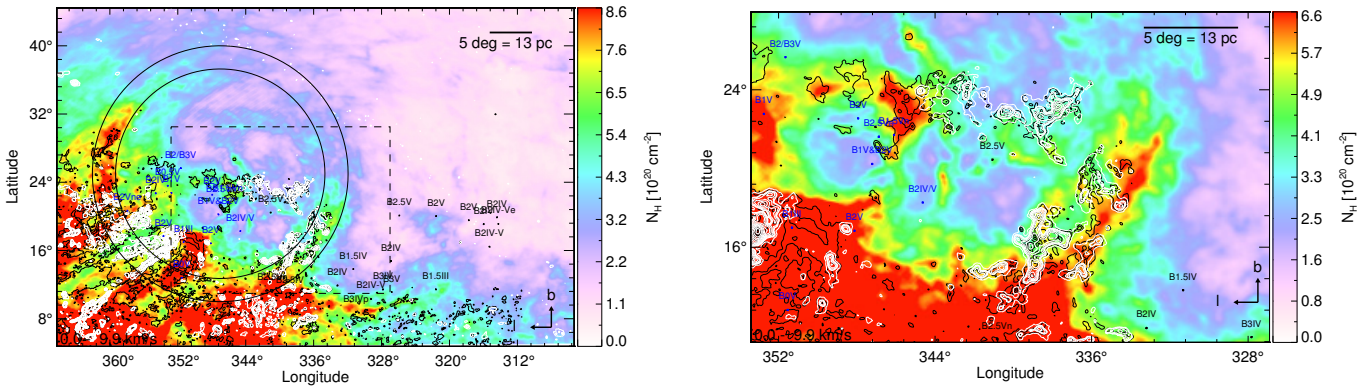

Fig. 8. *Left:* H I column density map of USco and the surroundings of Lupus I calculated from the integrated emission for v_{LSR} = 0–10 km s^{-1}. The two black circles indicate the inner and outer radius of the USco shell from the model fit. The black and white contours represent the dust emission at 850 μm and the CO(1–0) emission from *Planck*, respectively. The blue and black labeled dots represent early B-type stars in USco and UCL, respectively. *Right:* Zoom into the region indicated as a dashed black box in the left panel.

nitude lower than the estimated total mass of the USco shell ($\sim 10^4$ M$_\odot$) as derived from the H I model fit. If the atomic gas was homogeneously distributed within the shell, then at least $\sim 10^3$ M$_\odot$ would have been swept up at the current position of Lupus I, enough to create a $\sim$ 100 M$_\odot$ molecular cloud, and similar to the estimate of the total cloud mass by Tachihara et al. (1996). Furthermore, the analysis of the LABOCA continuum data has revealed many pre- and protostellar cores (see Paper I). This suggests that the formation timescale of the cloud and the onset of star formation should be on the order of even less than 2 Myr which is still in agreement with the atomic-to-molecular transition timescale. The large-scale magnetic field is perpendicular to the Lupus I filament, i.e. pointing in the direction of the USco shell expansion. This might have favored the accumulation of cold, dense atomic gas along the field lines and promoted fast molecule formation (Matthews et al. 2014; Hartmann et al. 2001; Vázquez-Semadeni et al. 2011).

The slightly supersonic irregular motions we find are in excellent agreement with predictions for clumps formed by the thin shell instability (Vishniac 1983). 3D simulations explicitly predict such velocities in clumps formed dynamically in expanding supershells (Krause et al. 2013, Fig. 9). We thus have three pieces of evidence, the correspondence between bulk HI and molecular velocities, the spatial anti-correlation between molecular and atomic gas, and the magnitude of the irregular motions which supports the picture that the Lupus I molecular cloud has formed dynamically in the expanding USco supershell. Also X-ray observations suggest that the UCL wind bubble might be colliding with the USco H I shell right at the position of Lupus I, squeezing it in between (see Paper I). This wind bubble, probably still additionally pressurized by past supernova activity, might have provided a counter-pressure to the expanding USco shell and thus favored this position for an additional compression of the shell material. In this way a new molecular cloud could have been created there and it would explain why not more very young star forming clouds (except ρ Ophiucus that is believed to be pre-existing (e.g. Motte et al. 1998)) are seen distributed within the wall of the USco shell.
This view is also supported by the column density PDFs of the dust emission (see Paper I), with the double-peak profile over the whole extent of the cloud. Together with the dust column density map this shows that Lupus I consists of a dense layer in the center of the filament which is surrounded by much more diffuse material. Simulations have shown that this is consistent with the idea of a two-sided compression through colliding flows (see Matsumoto et al. 2015). Then the molecular cloud is created in a dense and thin sheet which is surrounded by the diffuse material of the colliding flows.
This picture does, however, not come without difficulties: A formation of molecular clouds in colliding supershells requires that the shells have the same pressure evolution (Ntormousi et al. 2011). Any pressure difference can lead to cloud ablation and might destroy such clouds within about 10^6 yr (Krause et al. 2013). Since Lupus I is located between USco and UCL, its position also agrees with the much more extended Sco-CMa stream (Bouy & Alves 2015). It is therefore also possible that pre-existing density enhancements played a role in the formation of Lupus I.
Thompson et al. (2012) detected an increase in star-forming sources at the rim of the shells of HII regions (or IR/Spitzer bubbles). Shells are commonly observed in the Milky Way and other galaxies, but most diffuse shells seen in HI or the infrared do not have obvious triggered star formation. Dense molecular shells and pillars around HII regions often do have such triggering (e.g. Elmegreen 2011). Several scenarios try to explain star formation associated with expanding shells such as the "Collect and Collapse" (e.g. Elmegreen & Lada 1977; Whitworth et al. 1994), or the "Radiative Driven Implosion" (Deharveng et al. 2010) or even the Enhancement of pre-existing Density substructures and subsequent Global Implosion (e.g. Palmeirim et al. 2017; Walch et al. 2015). The trans-sonic irregular motion in Lupus I can be explained by the Vishniac thin shell instability. This supports a picture where clumping and possibly molecular gas formation was going on for a while, but star formation only set in when an external compression, quite possibly due to a supernova, triggered it. This is also consistent with the double-peaked density PDF in Lupus I and the coeval onset of star formation in the nearby ρ Ophiucus cloud, which could have been triggered by the same event. If the star formation was also related to gradual transformation of gas collected in a shell, then it would be more difficult to understand the sudden and coeval onset of star formation in both, Lupus I and ρ Oph. Thus, the data support a more complex, multi-stage formation process for Lupus I than a simple collect and collapse scenario.

7. Summary and Conclusions

In this paper we presented new ^{13}CO(2–1) and C^{18}O(2–1) line observations of Lupus I with the APEX telescope at three distinct cuts at different parts of the cloud.

A comparison of our CO data to H I data yielded that the emission of both tracers lies in the same velocity range. Moreover, C^{18}O emission peaks located in the center-south of Lupus I coincide with deficits in H I emission whereas the position of the H I emission peak in the north shows a deficit in C^{18}O emission. This resembles two different stages in the transition between atomic and molecular material. In the north, a smaller fraction of atomic hydrogen has been converted into molecular hydrogen and subsequently into dense CO. Therefore, this part of the cloud is quiescent. The center-south of the cloud has instead enough molecular material to actively form stars. This could also be a consequence of the lower dust column density in the northern part of Lupus I, because a smaller amount of dust particles reduces the formation efficiency of molecular hydrogen and provides less shielding from destructive UV radiation.

A comparison of the large-scale H I, CO, and dust emission in the USco shell and in the vicinity of Lupus I revealed that the molecular gas is always found in regions of dust emission and both of those components are preferentially found behind the outer edge of the atomic shell, i.e. further inwards. This is the expected configuration for molecular gas being produced inside the expanding H I shell. The CO velocities of Lupus I are in the same range as the H I velocities of the USco shell and thus the cloud is co-moving with the shell what would agree with the formation from the shell material. The timescale of the transition between atomic and molecular gas in such a massive shell with $M \approx 10^4$ M$_\odot$ (estimated from our model fit to the H I data) was estimated to be $\sim 10^6$–10^7 yr. This is consistent with the age of the USco shell (~ 5 Myr) and the age of the young stellar objects in Lupus I (< 2 Myr). The UCL wind bubble on the western side of Lupus I is colliding with the USco H I shell at the position of Lupus I squeezing it in between. Thus, it acted as a counterpressure to the expanding USco shell and favored this position for an additional compression of the shell material. In this way a new molecular cloud was created there. This additional collisional pressure might explain why not more very young star forming clouds are seen distributed within the wall of the USco shell. We showed by a geometrical model that the observational data are in agreement with this idea. This model also indicated that Lupus I can be expanding with the USco shell and that the cloud is located at the edge of the inner shell.

We suggest that Lupus I was and is strongly affected by large-scale external compression originating from the expansion of the USco H I shell and the UCL wind bubble, and that the cloud was formed out of the atomic material swept up by the USco shell and is now expanding with the shell. Pre-existing gas structure and collision with the UCL wind bubble were likely decisive factors that enhanced a local inhomogeneity and the density in the USco shell at a position that favored the formation of Lupus I.

Acknowledgements. We would like to thank the referee for his/her constructive comments which helped to improve this paper. This work was supported by funding from Deutsche Forschungsgemeinschaft under DFG project numbers PR 569/10-1 and PR 569/10-2 in the context of the Priority Program 1573 "Physics of the Interstellar Medium". Additional support came from funds from the Munich Cluster of Excellence "Origin and Structure of the Universe". The *Herschel* spacecraft was designed, built, tested, and launched under a contract to ESA managed by the Herschel/Planck Project team by an industrial consortium under the overall responsibility of the prime contractor Thales Alenia Space (Cannes), and including Astrium (Friedrichshafen) responsible for the payload module and for system testing at spacecraft level, Thales Alenia Space (Turin) responsible for the service module, and Astrium (Toulouse) responsible for the telescope, with in excess of a hundred subcontractors. Based on observations obtained with *Planck* (`http://www.esa.int/Planck`), an ESA science mission with instruments and contributions directly funded by ESA Member States, NASA, and Canada. HIPE is a joint development by the *Herschel* Science Ground Segment Consortium, consisting of ESA, the NASA *Herschel* Science Center, and the HIFI, PACS and SPIRE consortia. This research has made use of the SIMBAD database, operated at CDS, Strasbourg, France. We acknowledge the use of NASA's *SkyView* facility (http://skyview.gsfc.nasa.gov) located at NASA Goddard Space Flight Center.

Appendix A: Calculations of gas temperatures and column densities

Appendix A.1: Excitation temperature

The excitation temperature can be calculated via

$$T_{\rm ex}(\tau) = \frac{T_\nu^{18}}{\ln\left\{1 + \left[\frac{T_{\rm peak}^{18}}{T_\nu^{18}}\left(1 - \exp(-\tau_{18})\right)^{-1} + J(T_{\rm bg})/T_\nu^{18}\right]^{-1}\right\}} \tag{A.1}$$

where

$$J(T) \equiv \frac{c^2}{2k_B\nu^2}\, B_\nu(T) = \mathrm{T}_\nu\,[\exp(\mathrm{T}_\nu/\mathrm{T}) - 1]^{-1} \tag{A.2}$$

$\mathrm{T}_\nu = \frac{\mathrm{h}\nu_0}{\mathrm{k_B}}$, and $T_{\rm bg} = 2.73$ K the temperature of the cosmic microwave background (CMB). Eq. A.1, A.2 are derived from the equations given in Wilson et al. (2012).

Table A.1. Constants of the ^{13}CO(2–1) and C^{18}O(2–1) lines that are needed for the calculations in this chapter. ν_0 is the line's rest frequency, $T_\nu = h\,\nu_0/k_B$, μ is the molecule's dipole moment, and $B_{\rm rot}$ its rotational constant.

Line	ν_0 [GHz]	T_ν [K]	μ [D]	$B_{\rm rot}$ [10^{10} Hz]
^{13}CO(2–1)	220.3986765	10.577469	0.122	5.509967
C^{18}O(2–1)	219.5603568	10.537236	0.110	5.489009

Appendix A.2: H_2 column density

For the calculation of the column density we used

$$N(\mathrm{C^{18}O}) = \frac{\tau_{18}}{1 - \exp(-\tau_{18})} f(T_{\rm ex}) \int T_{\rm mb}^{18}\, d\nu \tag{A.3}$$

from Carlhoff et al. (2013) where the functions $f(T_{\rm ex})$ and $Q(T_{\rm ex})$ are defined as

$$f(T_{\rm ex}) = \frac{3h}{8\pi^3\mu^2} Q(T_{\rm ex}) \left\{\left[(J(T_{\rm ex}) - J(T_{\rm bg})\right]\left[1 - \exp\left(-\frac{T_\nu^{18}}{T_{\rm ex}}\right)\right]\right\}^{-1} \tag{A.4}$$

$$Q(T_{\rm ex}) = \frac{k_B T_{\rm ex}}{J_u B_{\rm rot} h} \exp\left(\frac{B_{\rm rot} J_u (J_u + 1) h}{k_B T_{\rm ex}}\right) \tag{A.5}$$

with $J_u = 2$ the upper level of the $J = 2 \rightarrow 1$ transition, μ the molecule's dipole moment, and $B_{\rm rot}$ its rotational constant. The partition function $Q(T_{\rm ex})$ is approximated for a linear molecule

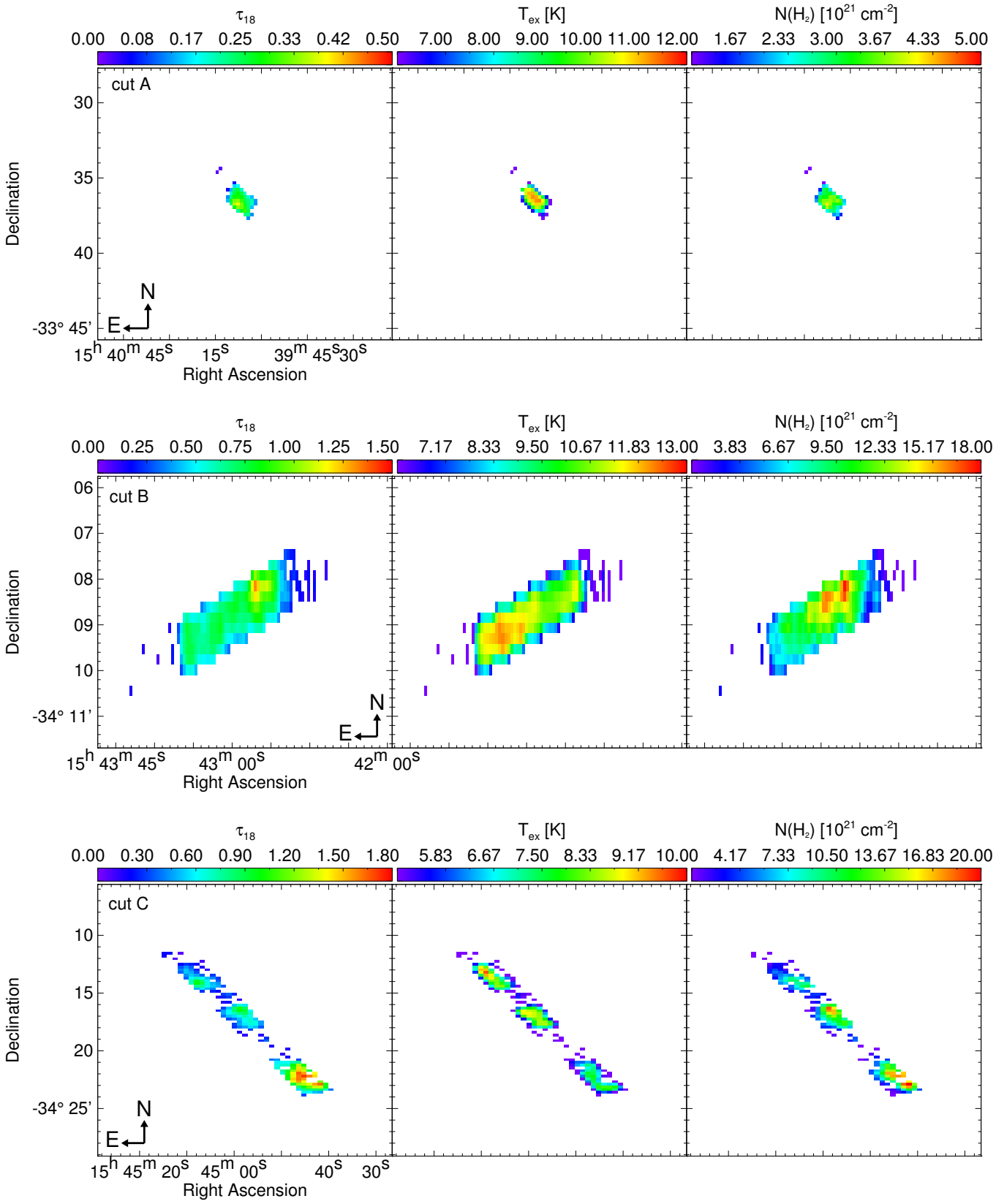

Fig. A.1. Results of the LTE analysis for cut A, B, and C (from top to bottom). The left panel shows the optical depth τ_{18}, the middle panel the excitation temperature T_{ex}, and the right panel the H_2 column density. All maps were convolved with a Gaussian of two pixels which corresponds approximatively to the beam size. Pixels within each cut for which the ^{13}CO(2–1) and the C^{18}O(2–1) spectrum had a S/N < 4 are left blank.

(Mangum & Shirley 2015). The factor $\tau_{18}/(1 - \exp(-\tau_{18}))$ corrects the integrated intensity for possible opacity broadening of

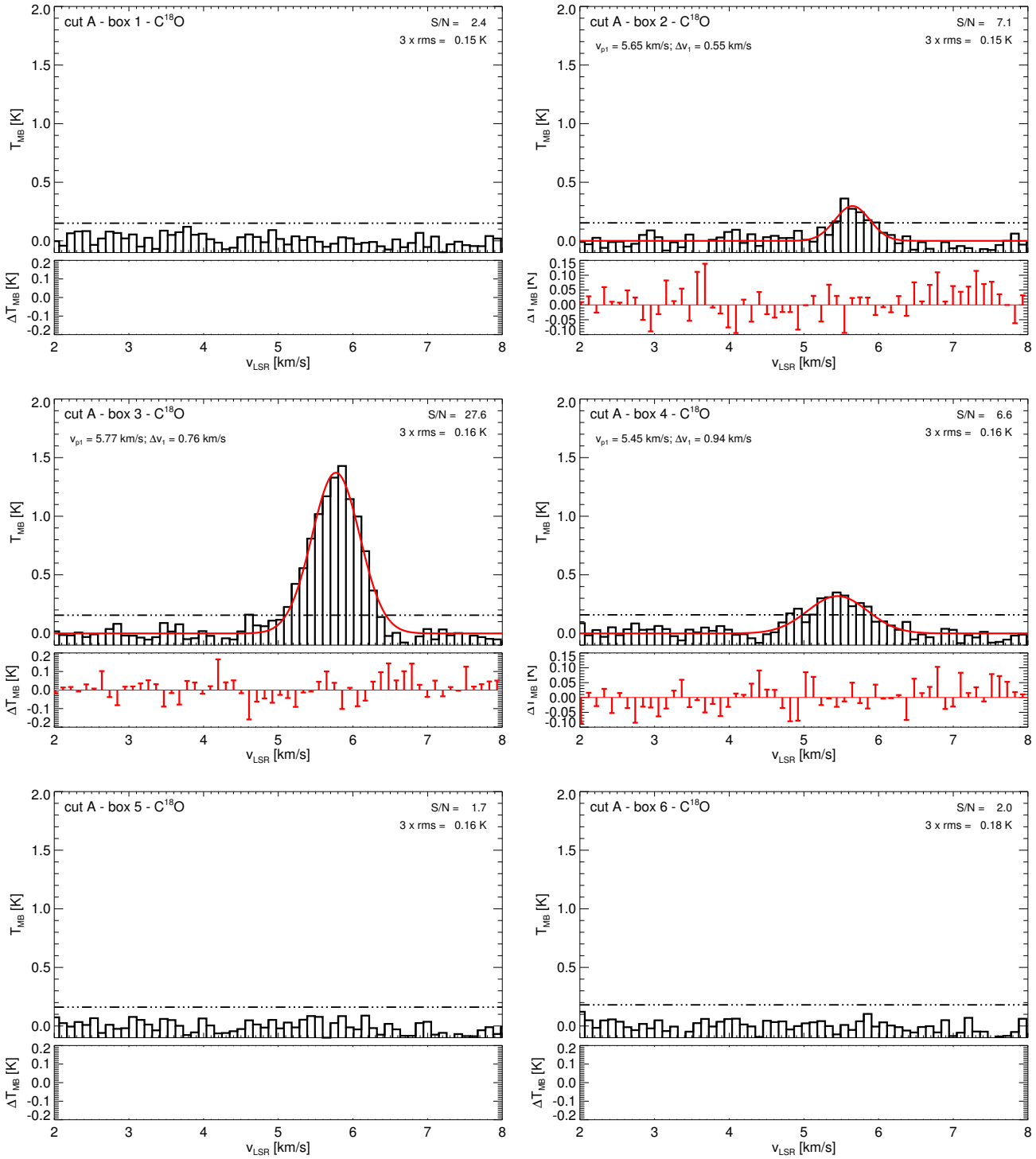

Fig. A.2. Histograms of the average $C^{18}O(2–1)$ spectra of the six boxes across cut A with a bin size of 0.1 km s^{-1}. The black dash-dotted line marks the 3 × rms limit. The values of 3 × rms and the signal-to-noise ratio S/N are given in the upper right of each plot. The red solid line shows the Gaussian fit to the spectrum. If more than one component was fitted, each one of them is represented by a blue dashed line and the red solid line is their sum. The residuals of the fit are given by the red bars in the small plot below each spectrum. Peak positions v_{p_i} and FWHM Δv_i of each component in one box are given in the upper left of each plot. A summary of all these values can be found in Table 2 where they are denoted by an upper index G.

the line (see Goldsmith & Langer 1999). But this effect should be in any case small for the $C^{18}O$ line because τ_{18} stays below unity in most pixels.

References

Benedettini, M., Pezzuto, S., Burton, M. G., et al. 2012, MNRAS, 419, 238

Benedettini, M., Schisano, E., Pezzuto, S., et al. 2015, MNRAS, 453, 2036

Bergin, E. A., Hartmann, L. W., Raymond, J. C., & Ballesteros-Paredes, J. 2004, ApJ, 612, 921

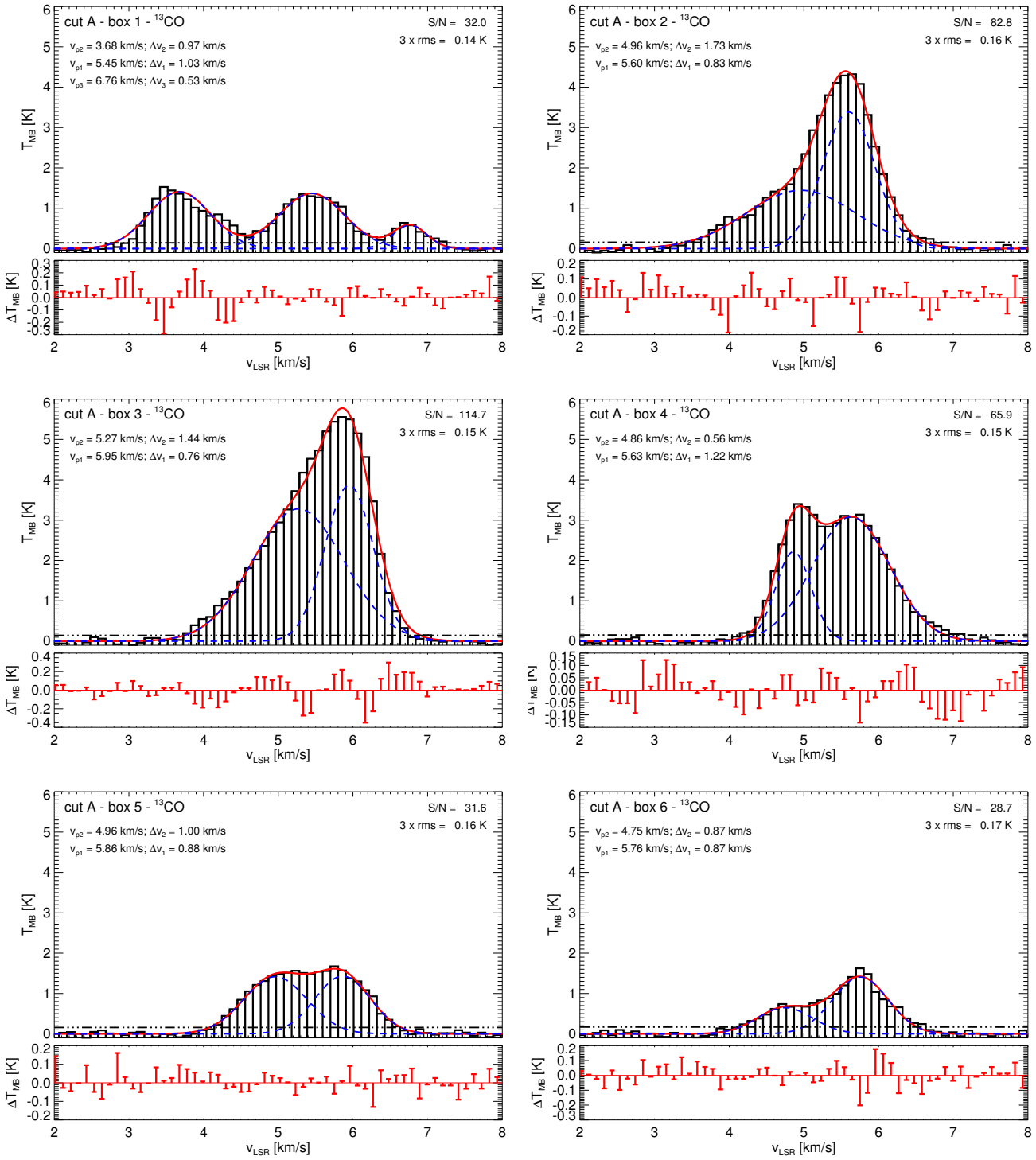

Fig. A.3. Histograms of the average ^{13}CO(2–1) spectra of the six boxes across cut A with a bin size of 0.1 km s^{-1}. The black dash-dotted line marks the 3 × rms limit. The values of 3 × rms and the signal-to-noise ratio S/N are given in the upper right of each plot. The red solid line shows the Gaussian fit to the spectrum. If more than one component was fitted, each one of them is represented by a blue dashed line and the red solid line is their sum. The residuals of the fit are given by the red bars in the small plot below each spectrum. Peak positions v_{p_i} and FWHM Δv_i of each component in one box are given in the upper left of each plot. A summary of all these values can be found in Table 2 where they are denoted by an upper index G.

Blaauw, A. 1964, in IAU Symposium, Vol. 20, The Galaxy and the Magellanic Clouds, ed. F. J. Kerr, 50
Bouy, H. & Alves, J. 2015, A&A, 584, A26
Calderón, D., Ballone, A., Cuadra, J., et al. 2016, MNRAS, 455, 4388
Carlhoff, P., Nguyen Luong, Q., Schilke, P., et al. 2013, A&A, 560, A24
Clark, P. C., Glover, S. C. O., Klessen, R. S., & Bonnell, I. A. 2012, MNRAS, 424, 2599
Comerón, F. 2008, Handbook of Star Forming Regions, Volume II, ed. Reipurth, B. (ed. B. Reipurth, ASP Monograph Publications), 295
Dawson, J. R., McClure-Griffiths, N. M., Kawamura, A., et al. 2011, ApJ, 728, 127
de Geus, E. J. 1992, A&A, 262, 258
de Zeeuw, P. T., Hoogerwerf, R., de Bruijne, J. H. J., Brown, A. G. A., & Blaauw, A. 1999, AJ, 117, 354

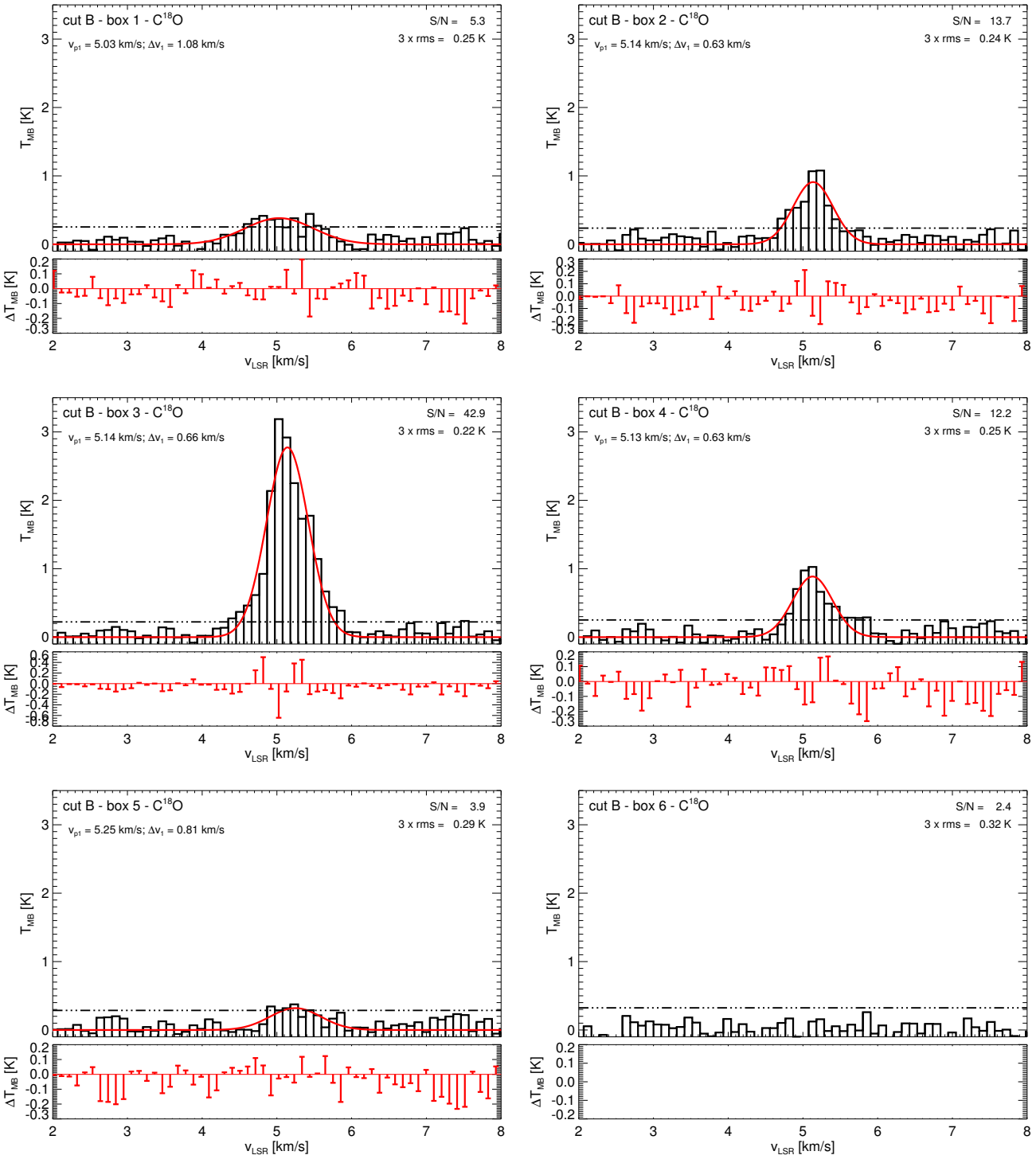

Fig. A.4. Same as Figure A.2 but for cut B.

Deharveng, L., Schuller, F., Anderson, L. D., et al. 2010, A&A, 523, A6
Dobbs, C. L., Krumholz, M. R., Ballesteros-Paredes, J., et al. 2014, Protostars and Planets VI, 1312.3223, 3
Elmegreen, B. G. 2011, in EAS Publications Series, Vol. 51, EAS Publications Series, ed. C. Charbonnel & T. Montmerle, 45–58
Elmegreen, B. G. & Lada, C. J. 1977, ApJ, 214, 725
Gaczkowski, B., Preibisch, T., Stanke, T., et al. 2015, A&A, 584, A36
Goldsmith, P. F. & Langer, W. D. 1999, ApJ, 517, 209
Güsten, R., Nyman, L. Å., Schilke, P., et al. 2006, A&A, 454, L13
Hacar, A. & Tafalla, M. 2011, A&A, 533, A34
Hara, A., Tachihara, K., Mizuno, A., et al. 1999, PASJ, 51, 895
Hartmann, L., Ballesteros-Paredes, J., & Bergin, E. A. 2001, ApJ, 562, 852
Haworth, T. J., Harries, T. J., Acreman, D. M., & Rundle, D. A. 2013, MNRAS, 431, 3470
Heiner, J. S., Vázquez-Semadeni, E., & Ballesteros-Paredes, J. 2015, MNRAS, 452, 1353
Heitsch, F. & Hartmann, L. 2008, ApJ, 689, 290
Kalberla, P. M. W., Dedes, L., Kerp, J., & Haud, U. 2007, A&A, 469, 511
Kalberla, P. M. W., McClure-Griffiths, N. M., Pisano, D. J., et al. 2010, A&A, 521, A17
Koyama, H. & Inutsuka, S.-I. 2000, ApJ, 532, 980
Krause, M., Fierlinger, K., Diehl, R., et al. 2013, A&A, 550, A49
Ladd, E. F., Fuller, G. A., & Deane, J. R. 1998, ApJ, 495, 871
Mangum, J. G. & Shirley, Y. L. 2015, PASP, 127, 266
Matsumoto, T., Dobashi, K., & Shimoikura, T. 2015, ApJ, 801, 77

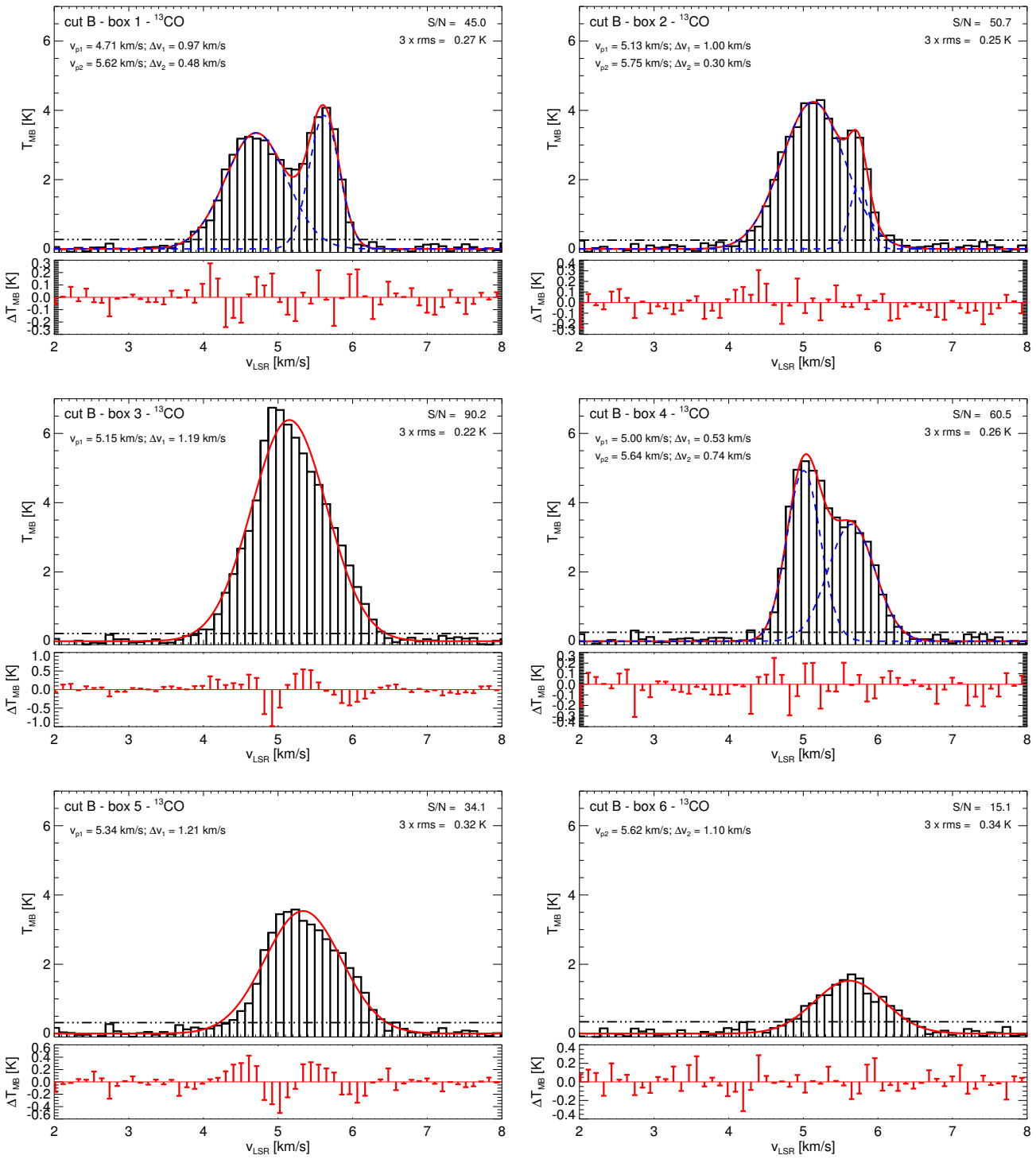

Fig. A.5. Same as Figure A.3 but for cut B.

Matthews, T. G., Ade, P. A. R., Angilè, F. E., et al. 2014, ApJ, 784, 116
Motte, F., Andre, P., & Neri, R. 1998, A&A, 336, 150
Myers, P. C. 1983, ApJ, 270, 105
Myers, P. C., Linke, R. A., & Benson, P. J. 1983, ApJ, 264, 517
Ntormousi, E., Burkert, A., Fierlinger, K., & Heitsch, F. 2011, ApJ, 731, 13
Palmeirim, P., Zavagno, A., Elia, D., et al. 2017, A&A, 605, A35
Phillips, T. G., Huggins, P. J., Wannier, P. G., & Scoville, N. Z. 1979, ApJ, 231, 720
Pöppel, W. G. L., Bajaja, E., Arnal, E. M., & Morras, R. 2010, A&A, 512, A83
Preibisch, T., Brown, A. G. A., Bridges, T., Guenther, E., & Zinnecker, H. 2002, AJ, 124, 404
Preibisch, T. & Mamajek, E. 2008, Handbook of Star Forming Regions, Volume II, ed. Reipurth, B. (ed. B. Reipurth, ASP Monograph Publications), 235
Tachihara, K., Dobashi, K., Mizuno, A., Ogawa, H., & Fukui, Y. 1996, PASJ, 48, 489
Tachihara, K., Toyoda, S., Onishi, T., et al. 2001, PASJ, 53, 1081
Thompson, M. A., Urquhart, J. S., Moore, T. J. T., & Morgan, L. K. 2012, MNRAS, 421, 408
Tothill, N. F. H., Löhr, A., Parshley, S. C., et al. 2009, ApJS, 185, 98
Vassilev, V., Meledin, D., Lapkin, I., et al. 2008, A&A, 490, 1157
Vázquez-Semadeni, E., Banerjee, R., Gómez, G. C., et al. 2011, MNRAS, 414, 2511
Vilas-Boas, J. W. S., Myers, P. C., & Fuller, G. A. 2000, ApJ, 532, 1038
Vishniac, E. T. 1983, ApJ, 274, 152
Walch, S., Whitworth, A. P., Bisbas, T. G., Hubber, D. A., & Wünsch, R. 2015, MNRAS, 452, 2794

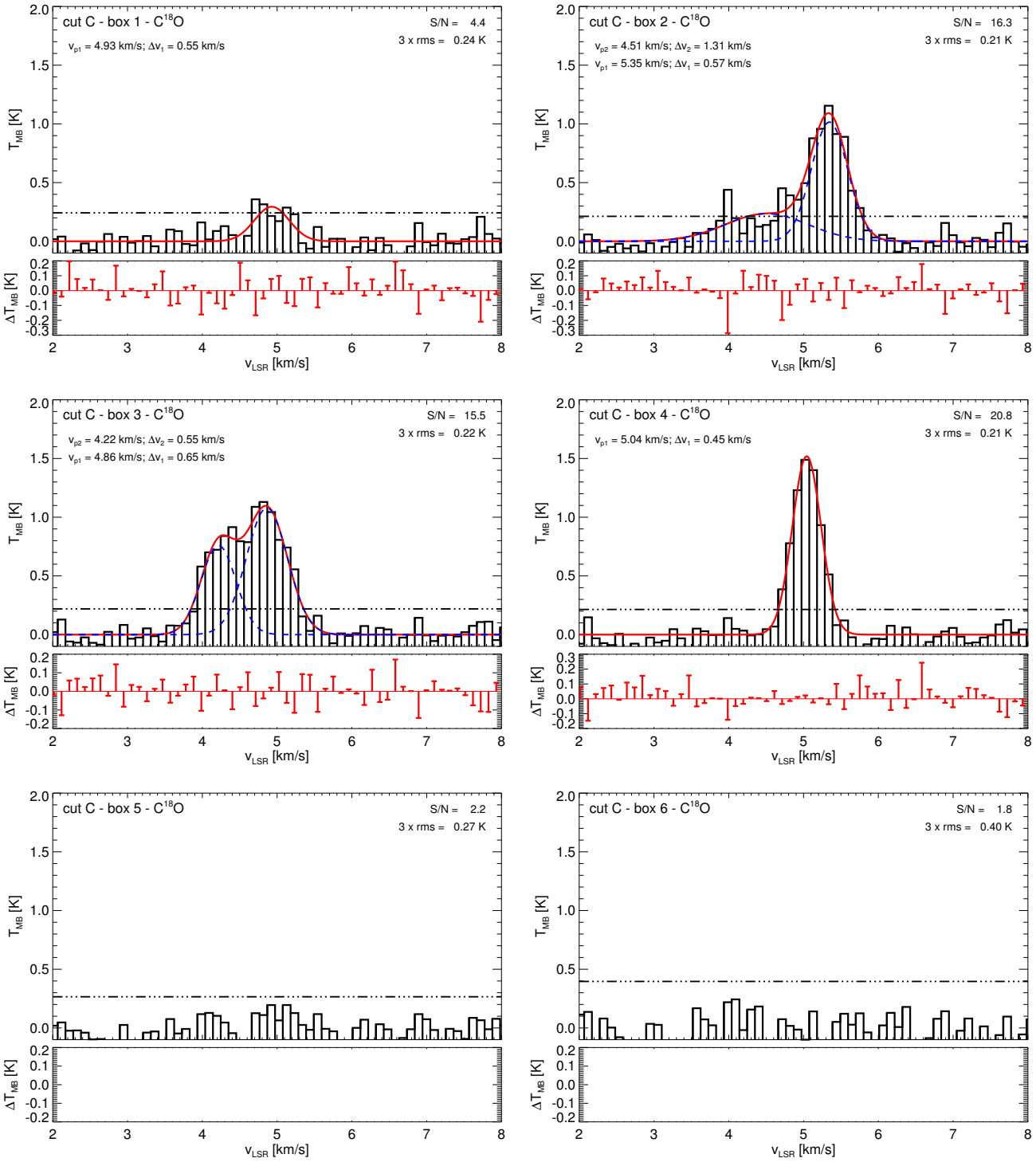

Fig. A.6. Same as Figure A.2 but for cut C.

Welsh, B. Y., Lallement, R., Vergely, J.-L., & Raimond, S. 2010, A&A, 510, A54

Whitworth, A. P., Bhattal, A. S., Chapman, S. J., Disney, M. J., & Turner, J. A. 1994, MNRAS, 268, 291

Wilson, T. L., Rohlfs, K., & Huttemeister, S. 2012, Tools of Radio Astronomy, 5th edition

Wilson, T. L. & Rood, R. 1994, ARA&A, 32, 191

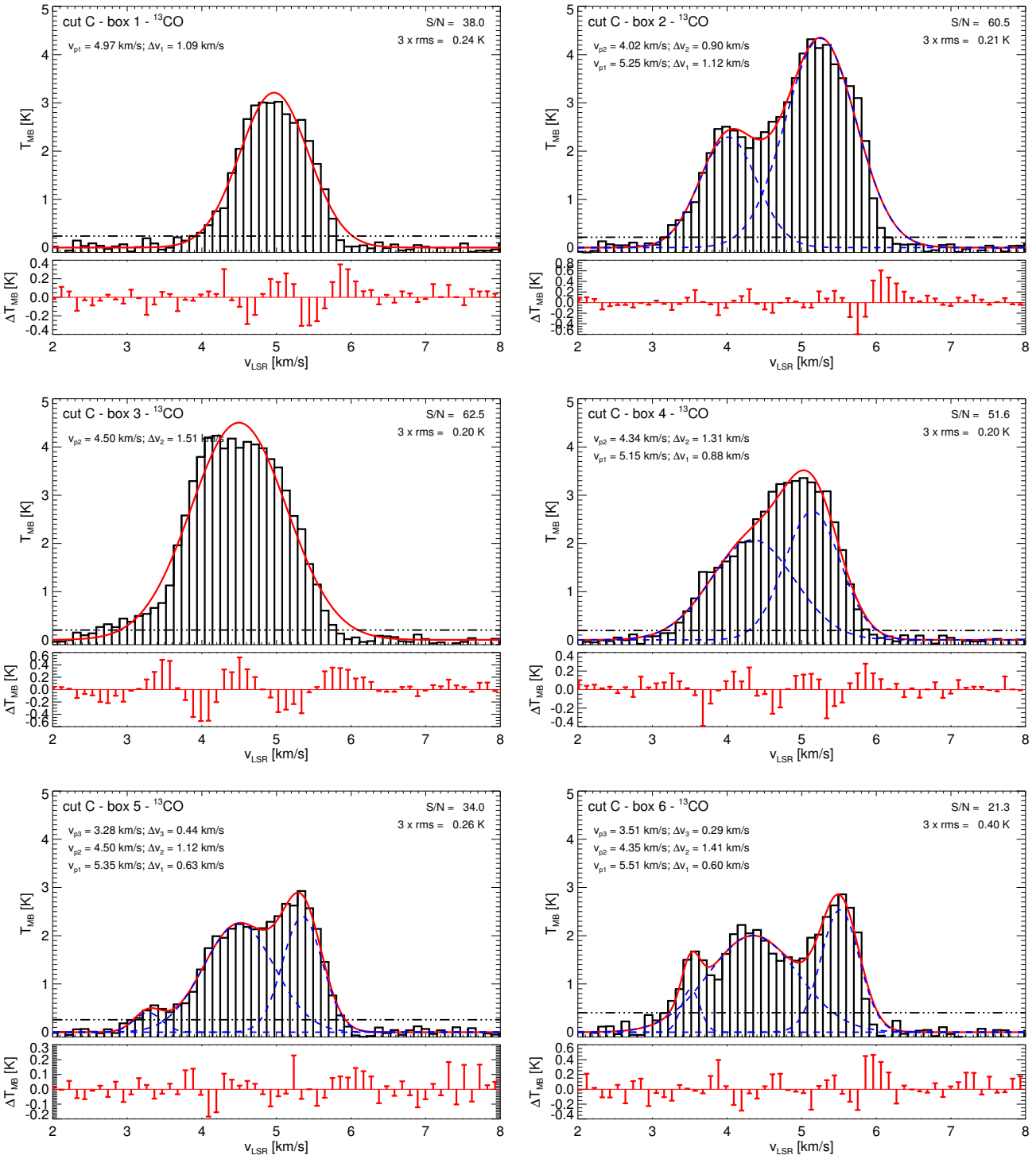

Fig. A.7. Same as Figure A.3 but for cut C.